

Unified Image Restoration and Enhancement: Degradation Calibrated Cycle Reconstruction Diffusion Model

Minglong Xue^a, Jinhong He^a, Shivakumara Palaiahnakote^b, Mingliang Zhou^c

^aCollege of Computer Science and Engineering, Chongqing University of Technology, Chongqing University of Technology, 400054, China

^bSchool of Science, Engineering and Environment, University of Salford, Manchester, UK

^cCollege of Computer Science, Chongqing University, Chongqing, 400044, China

Abstract

Image restoration and enhancement are pivotal for numerous computer vision applications, yet unifying these tasks efficiently remains a significant challenge. Inspired by the iterative refinement capabilities of diffusion models, we propose CycleRDM, a novel framework designed to unify restoration and enhancement tasks while achieving high-quality mapping. Specifically, CycleRDM first learns the mapping relationships among the degraded domain, the rough normal domain, and the normal domain through a two-stage diffusion inference process. Subsequently, we transfer the final calibration process to the wavelet low-frequency domain using discrete wavelet transform, performing fine-grained calibration from a frequency domain perspective by leveraging task-specific frequency spaces. To improve restoration quality, we design a feature gain module for the decomposed wavelet high-frequency domain to eliminate redundant features. Additionally, we employ multimodal textual prompts and Fourier transform to drive stable denoising and reduce randomness during the inference process. After extensive validation, CycleRDM can be effectively generalized to a wide range of image restoration and enhancement tasks while requiring only a small number of training samples to be significantly superior on various benchmarks of reconstruction quality and perceptual quality. The source code will be available at <https://github.com/hejh8/CycleRDM>.

Keywords: Image enhancement, Image restoration, Diffusion model.

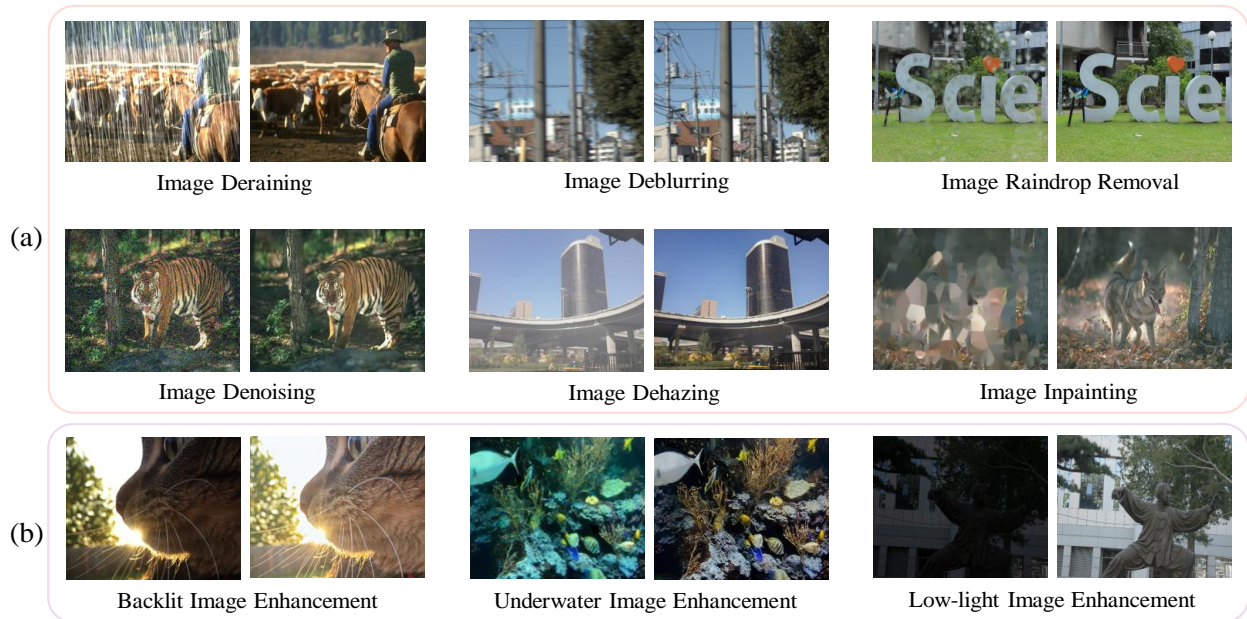


Figure 1: CycleRDM is capable of generating high-fidelity restoration in a variety of tasks. CycleRDM gives faithful results on a wide range of **(a)** linear image restoration tasks. Meanwhile, CycleRDM also realizes **(b)** blind, non-linear image enhancement tasks with high quality.

1. Introduction

Complex environmental conditions in the real world usually cause damage to the quality of captured images, leading to performance degradation in various computer vision applications, such as object detection [48]. Image restoration and enhancement aims to reverse the various degraded domains and restore the original clean image by learning the mapping relationship between the degraded and normal domains, thus improving the performance of various downstream tasks. In practice, most image restoration tasks are usually solved as linear inverse problems, such as image dehazing [31, 36], image deraining [40, 52], and image deblurring [28, 25], where the degradation model is usually linear and known. However, image enhancement tasks are more often studied as nonlinear blind problems, such as image low-light enhancement [42, 41], underwater image enhancement [2], and backlight image enhancement [18], where we need to simultaneously estimate the degradation model and recover clean images with high fidelity. Therefore, it is challenging to try to effectively unify the two types of tasks.

Along with the rise of deep learning, numerous researchers have been bridging the gap between degraded and normal images by learning powerful prior knowledge in large-scale datasets through a data-driven approach [15, 22, 42, 16]. However, existing advances are still challenged by the lack of ability to model various complex degradation conditions in the real world. Therefore, there has been a surge of interest in seeking broader prior knowledge of images through generative models [43, 46, 2]. Especially, recent diffusion models have received much attention (such as image restoration [3, 20, 21] and enhancement [11, 8, 23, 12]) for their impressive performance in image generation tasks. Specifically, diffusion models are trained to iteratively denoise the image by reversing a diffusion process to achieve a mapping from randomly sampled Gaussian noise to a complex target distribution without suffering from model collapse as GANs.

As a class of likelihood-based models, diffusion models model the details of the data through a large number of inference time steps in image generation tasks. For image restoration and enhancement tasks, we only need to repair the degraded regions in the given corrupted image, and thus adopting the image generation paradigm may lead to the generation of mismatched image details. Therefore, most of the existing methods [8, 11, 10] use fewer time steps (about 10 - 50 steps) to bridge the gap in the degraded domain through single-stage inference. However, the various degradation factors arising from complex real-world environments make it challenging to construct high-quality mappings with single-stage inference. This also complicates finding an efficient balance between linear degradation and blindness problems, leading to difficulties in developing high-quality, unified models for image restoration and enhancement tasks.

In this paper, we propose a Cycle Reconstruction Diffusion Model (CycleRDM) that performs fine-grained calibration of the degraded domain by employing a multi-stage diffusion inference process to achieve high-quality mappings from degraded images to normal images. This approach ensures the stable unification of image restoration and enhancement tasks. Specifically, we first learn the mapping relationships between the degraded domain to the rough normal domain and the rough normal domain to the fine normal domain through a two-stage diffusion inference process. Subsequently, we use the prior learned knowledge

to guide the final calibration process. In particular, inspired by [10, 11], we transfer the final calibration process to the wavelet low-frequency domain to achieve high-quality domain mapping from the frequency domain perspective and alleviate the consumption of computational resources. Meanwhile, we design a feature gain module using residual dense blocks to further remove redundant features from the wavelet high-frequency information in restoration tasks. To further stabilize the denoising process and minimize randomness during inference, we explore the use of multimodal text and Fourier transform-driven appearance reconstruction. As shown in Fig. 1, CycleRDM effectively unifies nine different types of degradation and produces visually appealing results. Extensive experiments show that CycleRDM achieves highly competitive performance, even with a limited amount of training data. Our main contributions are summarized below:

- We propose CycleRDM, which exploits the generative power of the diffusion model and combines it with the wavelet transform to construct a novel multi-stage diffusion inference process that achieves fine calibration and high-quality mapping of the degenerate domain using only a small amount of training data.
- We designed a feature gain module using residual dense blocks to further remove redundant features from the wavelet high-frequency information. In addition, we drive the reconstruction of the appearance and improve the stability of the inference process by combining multimodal text and Fourier transform.
- Through extensive experiments conducted on tasks involving nine different types of degradation, we demonstrate the effectiveness of CycleRDM. Our approach efficiently unifies image restoration and enhancement tasks, delivering highly competitive performance.

2. Related work

2.1. Image Restoration

Image restoration aims to achieve high-quality mapping of degraded images to normal images, which is a long-standing problem in computer vision and encompasses a variety of

tasks such as image denoising [39, 35], deraining [52, 40], dehazing [31, 47, 34], deblurring [17, 25]. Most of the existing methods focus on some single degradation task, using huge data-driven construction of high-quality mapping relations. However, recently, unified image restoration research has also begun to receive widespread attention [15, 1]. For example, NAFNet [1] derives a nonlinear activation-free network for multiple image restoration tasks by exploring the necessity of nonlinear activation functions. AIRNet [15] exploits the consistency of the same degraded image and the inconsistency present in different degradations to learn degradation representations for robust multi-task restoration. In addition, diffusion models [3, 21, 10] have also been widely used with impressive results due to their powerful generative capabilities. For example, IR-SDE [21] achieves good recovery results by constructing stochastic differential equations to reverse image degradation. WaveDM [10] Learning clean image distributions in the wavelet domain by performing wavelet transform embedded diffusion model to reduce the inference time overhead and achieved effective image recovery. However, despite their successes, these models still face limitations due to the lack of prior knowledge and the difficulty in modeling unknown degradation, which restricts them to linear image restoration tasks and limits their applicability to more complex, blind restoration problems.

2.2. Image Enhancement

Unlike most linear image restoration tasks, image enhancement tasks suffer from unknown degradation factors [3, 22]. Thus solving the blind inverse problem is not trivial, as one would need to simultaneously estimate the degradation model and recover a clean image with high fidelity. To deal with these unknown degradation tasks, numerous corresponding studies have been developed, such as low-light image enhancement [42, 41, 16], underwater image enhancement [2, 9], and backlit image enhancement [18]. Motivated by the power of the latest diffusion models in capturing and modifying data distributions and features, researchers have gradually explored the potential of generative paradigms to bridge the gap between unknown degradation domains [23, 11, 2]. For example, GSAD [8] leads to robust and effective low-light enhancement by establishing a global regularisation embedded in the

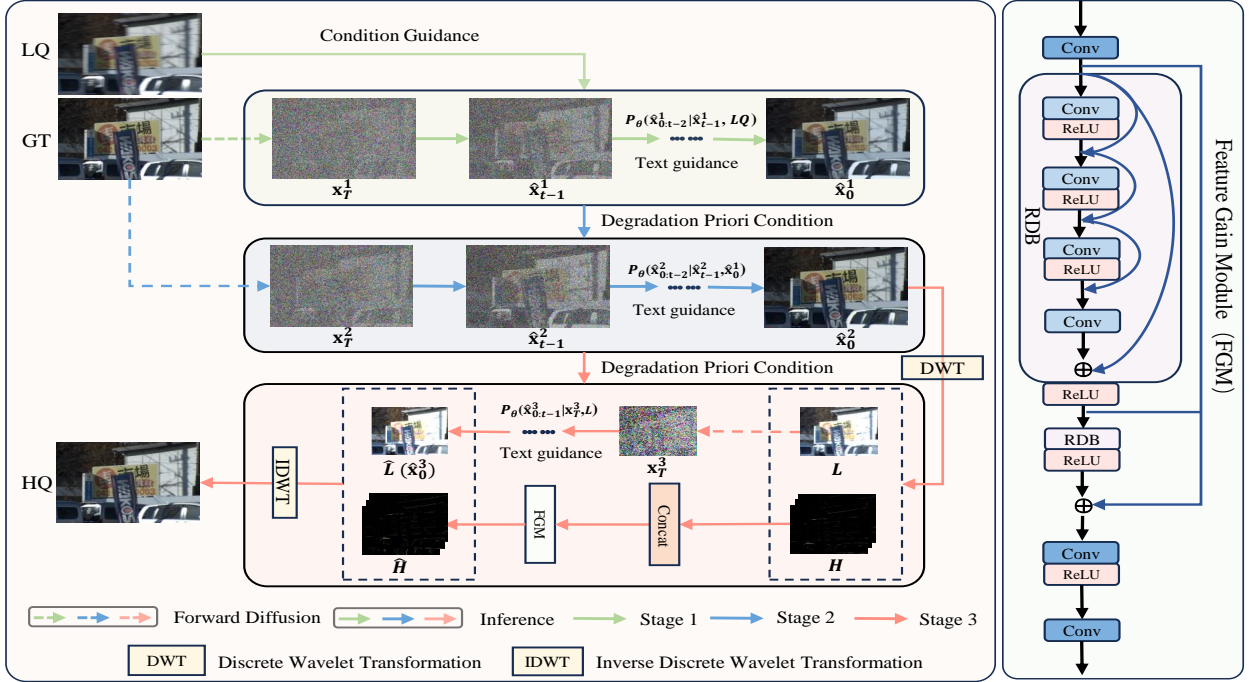


Figure 2: The proposed overall framework for CycleRDM. We use image deblurring as a demonstration. Firstly, in Stage 1 we use the degraded image LQ as a condition guidance to learn the mapping relation between the degraded domain to the rough normal domain, and later to guide the learning of the rough normal domain to the normal domain in Stage 2. In Stage 3, we perform a discrete wavelet transform (DWT) on the output \hat{x}_0^2 of stage 2. At the same time, a fine calibration is performed in the wavelet low-frequency domain L using the degradation prior learned earlier. For each Stage output, we also utilise multimodal text for appearance guidance. And the high-frequency H is enhanced by the feature gain module (FGM), and finally recovered to a high-quality image HQ by the inverse discrete wavelet transform ($IDWT$).

diffusion process. LightenDiffusion [12] performs self-consistent enhancement effects by incorporating Retinex theory in the diffusion latent space. GDP [3] proposed to use diffusion priors to generate realistic output and use this to connect image restoration and enhancement tasks. However, due to model limitations, these methods suffer from significant time overhead while failing to strike a stable balance between linear and blind problems, resulting in still task-biased model performance. In addition, recent DA-CLIP [22] utilizes image controllers to predict degradation and adjust a fixed CLIP image encoder to unify image restoration and enhancement, but it still rely on large amounts of training data and face challenges in generating high-quality images.

3. METHODOLOGY

In this study, we aim to explore diffusion models with fine calibration of degraded domains to unify image restoration and enhancement tasks effectively, significantly reduce the performance bias when the task is expanded, and enhance the stability of the model effect. Specifically, as shown in Fig. 2, we use deblurring as a demonstration example, and CycleRDM uses a three-stage diffusion inference process to gradually learn the mapping from a degraded domain to a normal domain with fine calibration. In addition, we further refine the features by designing a feature gain module to remove redundant features from the wavelet high-frequency information. Finally, multimodal text and the Fourier frequency domain are used to drive appearance reconstruction further and reduce content randomness in the inference process. In the following sections, we will elaborate on the proposed method.

3.1. Diffusion models Preliminary

Diffusion models to train Markov chains by variational inference. It converts complex data into completely random data by adding noise and gradually predicts the noise to recover the expected clean image. Consequently, it usually includes the forward diffusion process and reverse inference process.

The forward diffusion process mainly relies on incremental introduction of Gaussian noise with fixed variance $\{\beta_t \in (0, I)\}_{t=1}^T$ into the input distribution x_0 until the time steps of T approximate purely noisy data. This process can be expressed as:

$$q(x_t|x_{t-1}) = N(x_t; \sqrt{1 - \beta_t}x_{t-1}, \beta_t I), \quad (1)$$

where x_t and β_t are the corrupted noise data and the predefined variance at time step t . Respectively, N denotes a Gaussian distribution. Furthermore, each time step x_t of the forward diffusion process can be obtained directly by computing x_0 :

$$x_t = \sqrt{\bar{\alpha}_t}x_0 + \sqrt{1 - \bar{\alpha}_t}\epsilon, \quad \epsilon \sim N(0, I), \quad (2)$$

where $\alpha_t = 1 - \beta_t$, $\bar{\alpha}_t = \prod_{i=1}^t \alpha_i$.

The reverse inference process is to recover the original data from Gaussian noise. In contrast to the forward diffusion process, the reverse inference process relies on optimizing the noise predictor to iteratively remove the noise and recover the data until the randomly sampled noise $x_T \sim N(0, I)$ becomes clean data \hat{x}_0 . Formulated as:

$$p_\theta(\hat{x}_{t-1}|\hat{x}_t) = N(\hat{x}_{t-1}; \mu_\theta(\hat{x}_t, t), \sigma_t^2 I), \quad (3)$$

where μ_θ is the diffusion model noise predictor, which is mainly optimized by the editing and data synthesis functions and used as a way to learn the denoising process, as follows:

$$\mu_\theta = \frac{1}{\sqrt{\alpha_t}}(x_t - \frac{\beta_t}{\sqrt{1 - \alpha_t}}\epsilon_\theta(x_t, t)), \quad (4)$$

where ϵ_θ is a function approximator intended to predict noise vectors ϵ from \hat{x}_t .

3.2. Multi-Stage Diffusion Inference Process

In the single-stage denoising process of the diffusion model, the content diversity caused by randomly sampled noise is undesirable for image restoration and enhancement tasks, which will lead to instability in their performance. To address this, we propose stabilizing the model by gradually learning the gap between the degraded and normal domains through a multi-stage process. Additionally, we guide the calibration process using the learned degraded prior, which helps ensure more consistent and reliable performance.

Concretely, we first input the low-quality degraded image LQ as a condition in Stage 1, and map the degraded domain into the rough normal domain through diffusion inference. Where a Prior knowledge of some of the degraded parameters is stored through the initially recovered image \hat{x}_0^1 . Subsequently, in Stage 2, we use the \hat{x}_0^1 as a conditional input to further bridge the gap between the rough normal domain and the normal domain using the degradation parameters learned in Stage 1. Where, as inputs are made at each stage, we simultaneously use multimodal text to guide them through the stages. Especially in stage 1 and stage 2, we only set the time step of the forward diffusion process to 200. Meanwhile, the inverse denoising distribution is rewritten as conditional distribution:

$$p_\theta(\hat{x}_{0:T}|y) = p(\hat{x}_T) \prod_{t=1}^T p_\theta(\hat{x}_{t-1}|\hat{x}_t, y), \quad (5)$$

where y is the input image condition. The function approximator $\epsilon_\theta(x_t, t)$ becomes $\epsilon_\theta(x_t, t, y)$.

Finally, we use the output \hat{x}_0^2 in Stage 2 as a corrupted observation of the normal image GT . Furthermore, inspired by [11], we transfer Stage 3 to the low-frequency wavelet domain to calibrate the degradation and to alleviate the consumption of computational resources. Specifically, we employ the discrete wavelet transform $DWT(\cdot)$ which decomposes \hat{x}_0^2 into low-frequency information L and high-frequency information H .

$$\{L, H\} = DWT(\hat{x}_0^2), \quad (6)$$

where L contains the main information about the structure of the image content and H contains three high-frequency subbands in vertical, horizontal and diagonal directions.

In addition, due to the characteristics (Eq. 2) of the forward diffusion process, we perform diffusion and inference simultaneously in all three stages. Notably, we can perform fewer forward diffusion time steps in the third stage to obtain more conditional priors. With the prior degradation learned in the previous stages, L a refined calibration fine-tuning of 10 steps in the wavelet domain removes redundant information, resulting in a high-quality mapping. Thus, the overall optimization objective of the denoising network can be formulated as:

$$\mathcal{L}_{diff} = \sum_{s=1}^3 \tau_s \sum_{t=0}^T \mathbb{E}_s [\| \epsilon_t - \epsilon_\theta(x_t, t, y) \|_2], \quad (7)$$

where s is the stage of the diffusion inference process. τ_s is the weight parameter optimized by the noise reducer at each stage, which we set to $\tau_{s=1,2} = 1$ and $\tau_{s=3} = 0.9$.

3.3. Feature Gain Module

To further obtain the image restoration task performance, a feature gain module is designed for the wavelet high-frequency information decomposed by the calibration process, as shown in Fig. 2. Redundant features are further removed by combining the residual dense blocks (RDB) [35] and wavelet transform. Specifically, we first extract shallow features through a convolutional layer with a convolutional kernel size of 5×5 . Subsequently, a combination of 4-layers of RDB and ReLU was used to refine the features in the image further. At the same time, we fused the extracted features by two residual operations to

enhance the memory ability of shallow features to deeper ones to prevent long-term dependency. Finally, we again refine the extracted features and reconstruct the noise mapping by a combination of convolutional layers and ReLU. By removing the learned noise mappings, we further reconstruct H into clean high-frequency information \hat{H} . In this paper, the number of input channels and output channels of both RDBs is 64, the number of input channels of the last convolutional layer is 64, and the number of output channels is 3. Meanwhile, based on the enhanced high-frequency information \hat{H} and calibrated low-frequency information \hat{L} , we transform it into the final high quality recovered image HQ by inverse discrete wavelet transform $IDWT(\cdot)$:

$$HQ = IDWT(\hat{H}, \hat{L}). \quad (8)$$

3.4. Appearance Guidance And Network Training

In CycleRDM, in addition to the objective function \mathcal{L}_{diff} used to optimize the diffusion model, We also utilize multimodal text combined with a multi-stage process to construct a multi-level semantic guidance network that drives appearance reconstruction and process inputs at each stage through a frozen CLIP model. Specifically, for the outputs of each inference stage $\sum_{s=1}^3 \hat{x}_0^s$, we encode textual prompts by input pairing, which promotes recovery results close to positive prompts and away from negative prompts by performing computing semantic similarities in the CLIP latent space. Compared to most existing methods that use image-level supervised outputs, we supervise image generation at both semantic and appearance levels separately, effectively bridging the gap between metric-favorable and visually friendly and reducing model training obfuscation. We can represent this as:

$$\mathcal{L}_{clip} = \sum_{s=1}^3 \frac{e^{\cos(\Phi_{image}(\hat{x}_0^s), \Phi_{text}(T_n))}}{\sum_{j \in \{T_p, T_n\}} e^{\cos(\Phi_{image}(\hat{x}_0^s), \Phi_{text}(T_j))}}, \quad (9)$$

where T_p denotes positive prompts text (such as high light images), T_n denotes negative prompts text (such as low light images), Φ_{text} denotes text encoder, and Φ_{image} denotes image encoder. Furthermore, we utilize a content loss $\mathcal{L}_{content}$ that combines the MSE loss and the SSIM loss, in order to minimize the content difference between the recovered image

and the normal image:

$$\begin{aligned} \mathcal{L}_{content} = & \sum_{s=1}^3 \sum_{l=0}^4 \omega_l \|\Phi_{image}^l(\hat{x}_0^s) - \Phi_{image}^l(GT)\|_2 \\ & + (1 - SSIM(HQ, GT)), \end{aligned} \quad (10)$$

where ω_l is the weight of layer l of the image encoder in the ResNet101 CLIP model. We set $\omega_{l=0,1,2,3} = 1$ and $\omega_{l=4} = 0.5$. Meanwhile, we introduce the frequency-aware loss \mathcal{L}_{fre} to learn the GT spectrum, which consists of two components: amplitude amp and phase pha :

$$amp_{hq}, pha_{hq} = \mathcal{F}_{df}(HQ), \quad (11)$$

$$amp_{gt}, pha_{gt} = \mathcal{F}_{df}(GT), \quad (12)$$

$$\mathcal{L}_{fre} = \vartheta_1 \|amp_{hq} - amp_{gt}\|_1 + \vartheta_2 \|pha_{hq} - pha_{gt}\|_1, \quad (13)$$

where \mathcal{F}_{df} denotes the fast Fourier transform (FFT), ϑ_1 and ϑ_2 are the weighting parameters for amplitude loss and phase loss and were all set to 0.5 based on experience.

Thus, the total training loss can be defined as:

$$\mathcal{L}_{total} = \mathcal{L}_{diff} + \gamma_1 \mathcal{L}_{clip} + \mathcal{L}_{content} + \gamma_2 \mathcal{L}_{fre}, \quad (14)$$

where γ_1 and γ_2 are hyperparameters set to 0.2 and 0.3, respectively.

4. EXPERIMENTS

In this section, we describe the implementation details, datasets in detail. We validate the generalization of CycleRDM by performing a systematic comparison of CycleRDM on a series of different tasks after training. In particular, compared to other baselines, we select only a small number of training samples of no more than 500 in each different dataset. We also conduct a series of ablation experiments to validate the effectiveness of the proposed design.

Table 1: Details of the number of images we selected for training and testing for each task.

Image Number	Dehazing	Deraining	Deblurring	Denoising	Raindrop Remova	Inpainting	Low-light	Underwater	Backlight
Train Phase	500	500	500	500	500	500	485	500	0
Test Phase	1000	100	50	68	58	100	170	50	30

4.1. Datasets

We provide detailed information about the dataset for all tasks. For each task’s dataset, as shown in Table 1, we select only a small number of random images (up to 500) for training and test them uniformly on the test set. Compared to the baseline DA-CLIP and IR-SDE we greatly alleviate the training data and achieve superior performance. Therefore, for each task, in addition to the two baselines of unified image recovery methods, we compare more with the state-of-the-art methods for the particular task. The details are as follows:

- **Image Deraining:** We use the Rain100H dataset [44] for training and testing. This is a synthetic dataset containing 1800 paired training images and 100 test images. Among them, We randomly selected 500 images to add to the training data and compared them on 100 test sets.
- **Image Dehazing:** We use the RESIDE-6k dataset [31] for training and testing, which is a mixture of indoor and outdoor images, with 6000 images for training and 1000 images for testing. In particular, we select only a small number of 500 images for training.
- **Image Denoising:** We trained on 500 randomly selected images from other task datasets, but all LQ images were generated by adding Gaussian noise at noise level 50. The test images are from CBSD68 [26], a dataset with 68 denoised images and Gaussian noise added.
- **Image Deblurring:** We use the GoPro for training as other methods and validate on the BSD dataset [54]. In this case, the training images are still only 500, and we randomly select 50 from the BSD dataset for the test images.
- **Image Raindrop Removal:** We use the RainDrop dataset [30], which contains 861 images for training and 58 images for testing.

- **Image Inpainting:** We use 256-resolution images from CelebaHQ as the training dataset, which contains 30,000 images, and We used 500 images to add to the training data and 100 images segmented using 100 thin masks in RePaint [20] for testing. In addition, we also take a random masking process for some of the images used for testing.
- **Low-light Image Enhancement:** We use the LOLv1 dataset [38] for training, which contains 485 paired images for training and 15 images for testing. Also, we test directly on the LOLv2-real dataset [45], which contains 100 test images. In addition, we test on the unpaired datasets LIME [6] and DICM [14].
- **Backlight Image Enhancement:** We randomly selected 30 images from the Back-Lit300 dataset [18] for testing.
- **UnderWater Image Enhancement:** We use the LSUI dataset [29], consisting of 5004 image pairs, which involves richer underwater scenes (lighting conditions, water types, and target classes) and better visual quality reference images than the existing ones. The test data were randomly selected from 50 images, and the training images were randomly selected from 500 images.

4.2. Implementation Details

We implemented our method on two NVIDIA Tesla V100s GPUs using PyTorch on an Ubuntu system. We performed a total of 1000 epochs on the network using the Adam optimizer, with the initial learning rate set to 1×10^{-4} , and the patch size set to 128×128 respectively. To achieve efficient recovery, In order to achieve efficient recovery, time steps were set to 200 for the training phase, and for the denoising phase, the implicit sampling step was set to 10.

4.3. Image Restoration Tasks

To quantify the performance of CycleRDM, we show the evaluated effects of four specific degradation tasks: image deraining on the Rain100H dataset [44]; image denoising on the CBSD68 dataset [26]; image deblurring on the BSD dataset [54]; image dehazing on the

Table 2: Quantitative comparison of our method with other state-of-the-art methods between four different image restoration tasks. The best and second performance are marked in red and blue, respectively.

(a) Dehazing Quantitative comparison on the RESIDE-6k dataset. (b) Denoising Quantitative comparison on the CBSD68 dataset.

Methods	Reference	RESIDE-6k				Methods	Reference	CBSD68			
		PSNR \uparrow	SSIM \uparrow	LPIPS \downarrow	FID \downarrow			PSNR \uparrow	SSIM \uparrow	LPIPS \downarrow	FID \downarrow
FFANet [31]	AAAI'20	20.766	0.891	0.084	9.112	DBSN [39]	ECCV'20	26.456	0.713	0.281	107.972
MSFNet [55]	TIP'21	23.931	0.914	0.071	10.166	DCDiL [53]	CVPR'21	28.565	0.786	0.235	83.128
MAXIM [36]	CVPR'22	29.121	0.932	0.045	8.116	Restormer [49]	CVPR'22	27.246	0.762	0.215	87.140
IR-SDE [21]	ICML'23	25.250	0.908	0.062	8.330	AirNet [15]	CVPR'22	27.511	0.769	0.264	93.890
D4_plus [46]	IJCV'23	25.875	0.926	0.037	9.826	IR-SDE [21]	ICML'23	24.821	0.640	0.232	79.380
UME-Net [34]	PR'24	26.766	0.938	0.041	8.395	WCDM [11]	TOG'23	25.899	0.699	0.292	103.488
DA-CLIP [22]	ICLR'24	30.062	0.935	0.033	5.341	DA-CLIP [22]	ICLR'24	24.333	0.571	0.269	69.908
Ours	-	29.202	0.960	0.026	7.095	Ours	-	27.424	0.789	0.166	55.947

(c) Deblurring Quantitative comparison on the BSD dataset. (d) Deraining Quantitative comparison on the Rain100H dataset.

Methods	Reference	BSD				Methods	Reference	Rain100H			
		PSNR \uparrow	SSIM \uparrow	LPIPS \downarrow	FID \downarrow			PSNR \uparrow	SSIM \uparrow	LPIPS \downarrow	FID \downarrow
MTRNN [28]	ECCV'20	25.960	0.831	0.195	68.064	RecDerain [32]	TIP'20	29.016	0.899	0.104	45.698
DID-Anet [24]	TIP'21	25.573	0.803	0.243	71.122	MPRNet [50]	CVPR'21	28.519	0.872	0.152	62.146
MSDI-Net [17]	ECCV'22	27.049	0.859	0.145	49.351	NAFNet [1]	ECCV'22	27.322	0.853	0.149	46.350
NAFNet [1]	ECCV'22	25.336	0.797	0.266	69.268	IDT [40]	TPAMI'23	32.148	0.931	0.065	25.951
IR-SDE [21]	ICML'23	23.723	0.806	0.179	64.506	IR-SDE [21]	ICML'23	29.097	0.886	0.050	20.869
DeepRFT [25]	AAAI'23	28.995	0.901	0.143	47.421	WSDformer [52]	TMM'24	25.663	0.775	0.092	26.409
DA-CLIP [22]	ICLR'24	25.631	0.812	0.156	53.660	DA-CLIP [22]	ICLR'24	28.756	0.849	0.071	29.214
Ours	-	29.056	0.889	0.113	38.643	Ours	-	30.407	0.908	0.050	20.318

RESIDE-6K dataset [31]; image raindrop removal on the RainDrop dataset [30]; and image inpainting on the CelebaHQ dataset. For each experiment, we measure the fidelity of recovery performance and the quality of the resulting images using two distortion metrics, PSNR and SSIM [37], and two perceptual metrics, LPIPS [51] and FID [7].

Comparison Methods. For all tasks, due to the specificity of the training, we focus more on the comparison with the current state-of-the-art methods for the specific task, such as 1) DBSN [39], DCDiL [53], Restormer [49], WCDM [11] for image denoising; 2)

Table 3: Quantitative comparison of our method with other state-of-the-art methods in image inpainting and image raindrop removal tasks.

Tasks	Methods	Reference	PSNR \uparrow	SSIM \uparrow	LPIPS \downarrow	FID \downarrow
Inpainting	Restormer [49]	CVPR'22	29.881	0.914	0.068	31.960
	IR-SDE [21]	ICML'23	27.557	0.884	0.061	29.605
	GDP [3]	CVPR'23	32.028	0.889	0.046	28.318
	DA-CLIP[22]	ICLR'24	29.277	0.901	0.042	22.684
	Ours	-	30.292	0.926	0.039	22.053
Raindrop	AirNet [15]	CVPR'22	29.085	0.916	0.099	38.310
	IR-SDE [21]	ICML'23	28.191	0.836	0.107	34.221
	WaveDM [10]	TMM'24	28.905	0.866	0.113	36.321
	DA-CLIP [22]	ICLR'24	29.305	0.882	0.061	22.379
	Ours	-	29.857	0.908	0.058	28.879

RecDerain [32], MPRNet [50], IDT [40], WSDformer [52] for image deraining; 3) MTRNN [28], DID-Anet [24], MSDI-Net [17], DeepRFT [25] for image deblurring; 4) FFANet [31], MSFNet [55], the UME-Net [34] and D4-plus [46] for image dehazing. We also compare with IR-SDE [21] and DA-CLIP [22], which are two advanced image restoration network architectures for state-of-the-art performance on multiple tasks. In addition, for the image Inpainting and image raindrop removal tasks, we compare them with four image restoration methods, respectively.

Quantitative Results. Table 2 summarises the quantitative results for four different image restoration tasks. Our method is vastly superior in all recovery tasks, where we achieve the top two evaluation results for all tasks in the SSIM and perceptual evaluations, and set several state-of-the-art performances. In addition, we also achieved first place in the deblurring task and second place in the deraining and dehazing tasks in the PSNR evaluation. Compared to the baseline methods IR-SDE and DA-CLIP, our method overall improves the metrics results for all datasets, demonstrating better generalization performance and stability.

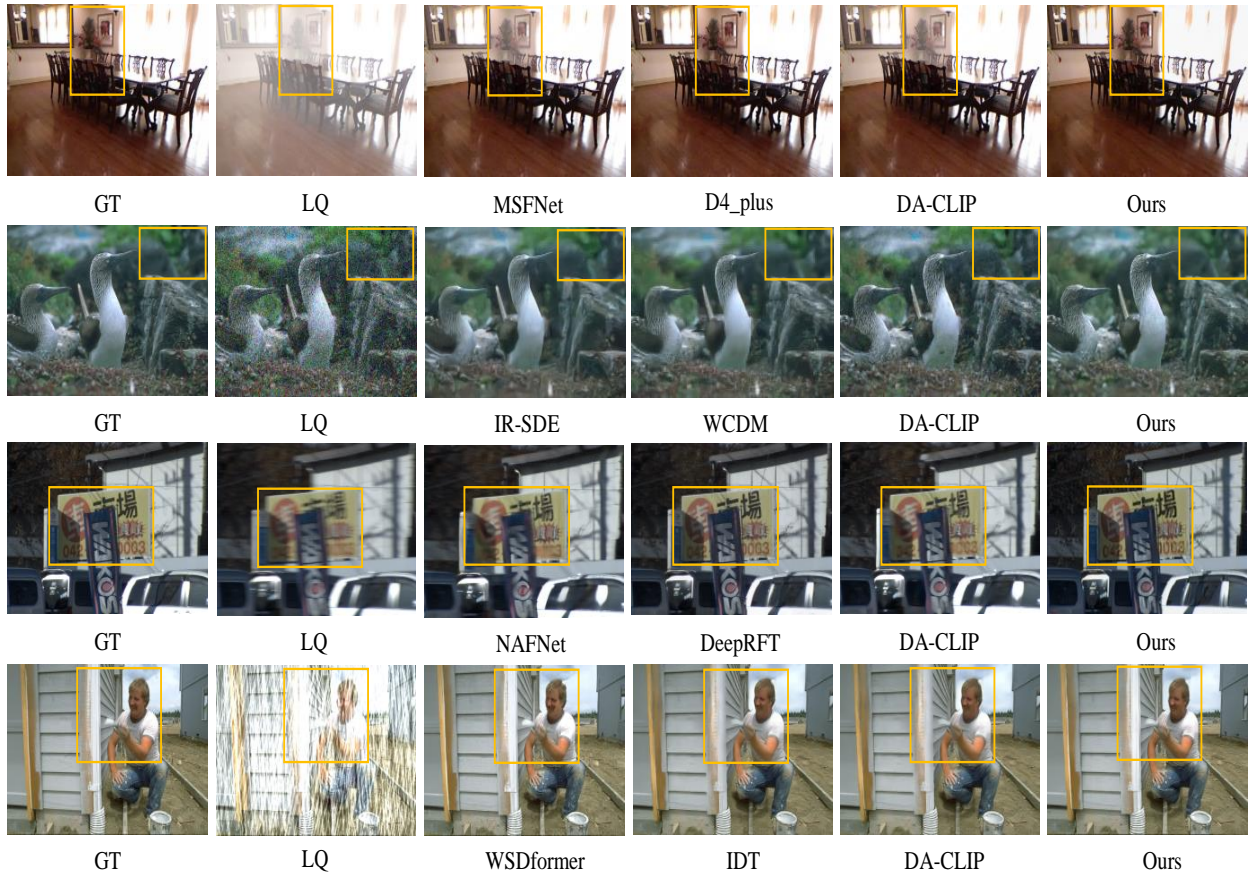


Figure 3: Comparison of our method with other methods on 4 different degradation-specific tasks. Where the first to fourth rows are dehazing, denoising, deblurring, and deraining respectively. Best viewed by zooming in.

In addition, Table 3 demonstrates the performance in the image inpainting and image raindrop removal tasks. Compared to the three multitasking image restoration methods, we obtained the best performance in the image inpainting task for SSIM, LPIPS and FID evaluations, and acquired the second place in the PSNR evaluation. In the image raindrop removal task on the other hand, we obtained the best performance evaluation in PSNR and LPIPS and the second place in SSIM and FID evaluation. This further demonstrates the generalisation ability of our method for linear image restoration tasks as well as better machine-aware results.

Qualitative Results. As shown in Fig. 3, we first show a visual comparison of the four tasks of de-fogging, de-noising, de-blurring and de-raining with a wide range of method-

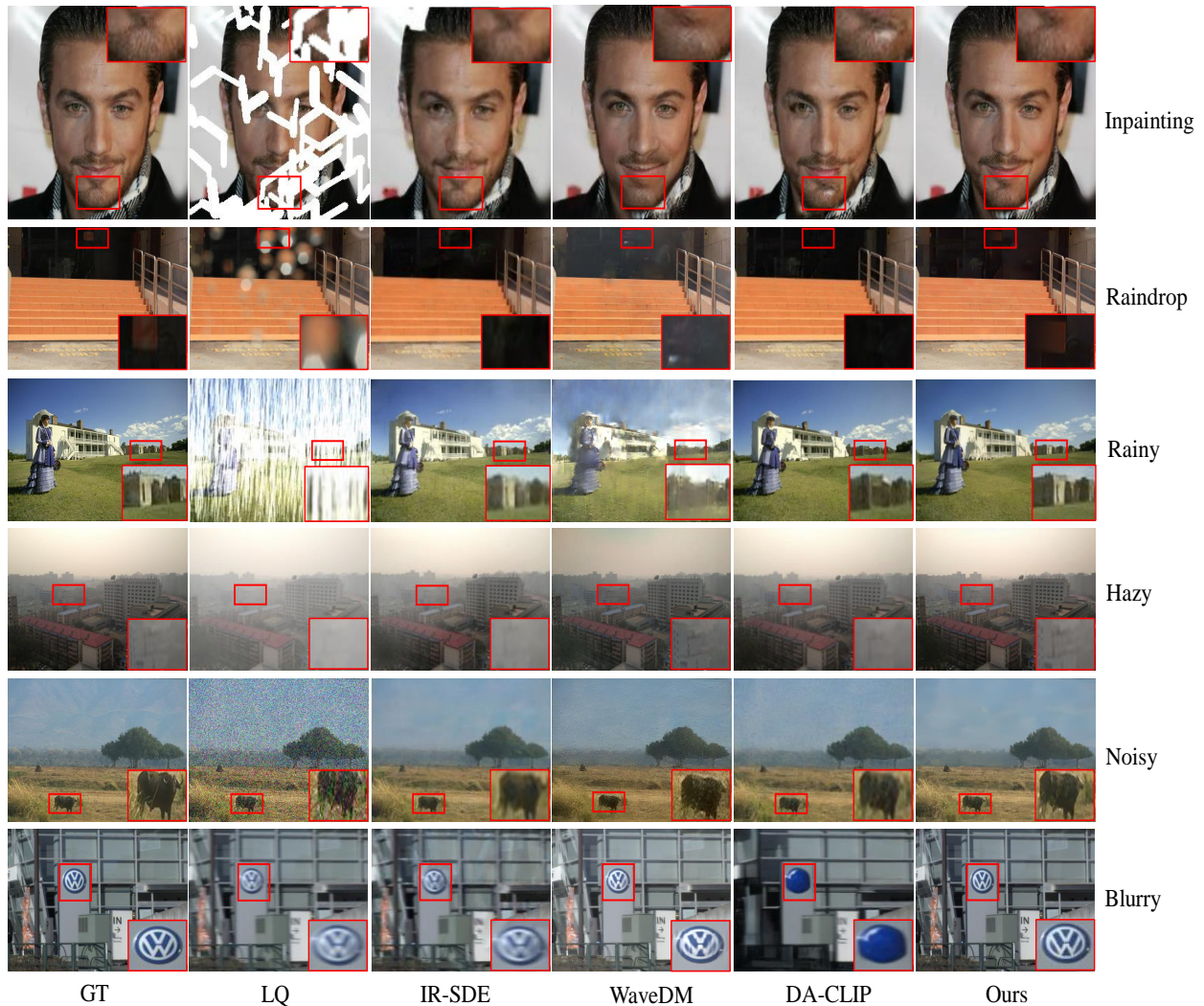


Figure 4: Comparison of our method with other state-of-the-art methods in image restoration tasks with different degradation types. Best viewed by zooming in.

specific experiments. It can be seen that our methods are clearly competitive in terms of details and overall visual effects. For example, in the de-fogging task, MSFNet and DA-CLIP cannot effectively remove white fog. In the deblurring task, we were able to further recover a clear visual effect. This further validates the effectiveness of CycleRDM to achieve a restoration effect that is more satisfying to human visual perception.

Also, we show a visual comparison with three multitasking methods IR-SDE, WaveDM and DA-CLIP on all image restoration tasks. As shown in Fig. 4, CycleRDM achieves

Table 4: Quantitative comparison of our method with other SOTA methods on low-light image enhancement image enhancement tasks. The best and second performance are marked in red and blue, respectively.

Methods	Reference	LOLv1						LOLv2_Real					
		PSNR↑	SSIM↑	LPIPS↓	FID↓	MUSIQ↑	VIF↑	PSNR↑	SSIM↑	LPIPS↓	FID↓	MUSIQ↑	VIF↑
SNRnet [42]	CVPR'22	24.309	0.841	0.262	56.467	65.225	0.488	21.480	0.849	0.237	54.532	62.506	0.536
NeRco [43]	ICCV'23	22.946	0.785	0.311	76.727	68.964	0.359	25.172	0.785	0.338	84.534	66.159	0.348
CLIP-LIT [18]	ICCV'23	12.394	0.493	0.397	108.739	57.099	0.434	15.262	0.601	0.398	100.459	55.904	0.456
GDP [3]	CVPR'23	15.904	0.540	0.431	112.363	60.585	0.380	14.290	0.493	0.435	102.416	58.381	0.424
UHDFour [16]	ICLR'23	23.095	0.822	0.259	56.912	59.019	0.487	21.785	0.854	0.291	60.849	66.023	0.536
GSAD [8]	NeurIPS'23	27.629	0.876	0.188	43.659	72.479	0.547	28.805	0.894	0.201	41.456	69.139	0.532
WCDM [11]	TOG'23	26.316	0.844	0.219	48.037	66.896	0.462	28.875	0.874	0.203	45.395	64.389	0.508
FourierDiff [23]	CVPR'24	17.560	0.607	0.359	77.768	57.289	0.485	17.304	0.783	0.303	63.499	54.299	0.503
LightenDiffusion [12]	ECCV'24	20.188	0.814	0.316	85.930	57.952	0.463	22.443	0.867	0.305	75.582	57.952	0.508
DA-CLIP [22]	ICLR'24	23.528	0.810	0.204	34.852	70.587	0.497	31.009	0.851	0.187	27.962	65.254	0.546
UPT-Flow [41]	PR'25	20.644	0.862	0.215	48.926	60.768	0.507	25.056	0.889	0.231	50.757	57.952	0.556
Ours	-	24.423	0.865	0.179	41.128	72.663	0.552	25.893	0.901	0.158	32.368	69.214	0.606

Table 5: Quantitative comparison of our method with other state-of-the-art methods between underwater image enhancement and backlight image enhancement tasks.

Methods	Reference	LSUI						Methods	Reference	Backlit300
		PSNR↑	SSIM↑	LPIPS↓	FID↓	MUSIQ↑	VIF↑			MUSIQ↑
TACL [19]	TIP'22	21.150	0.781	0.238	56.381	44.176	0.525	SNRnet [42]	CVPR'22	53.734
PUIE-Net [5]	ECCV'22	21.782	0.813	0.255	51.698	43.328	0.579	CLIP-LIT [18]	ICCV'23	63.141
USUIR [4]	AAAI'22	19.683	0.783	0.298	59.291	43.910	0.564	GDP [3]	CVPR'23	54.578
Semi-UIR [9]	CVPR'23	22.054	0.814	0.194	50.115	51.311	0.645	UHDFour [16]	ICLR'23	59.587
PUGAN [2]	TIP'23	22.507	0.816	0.215	51.622	45.481	0.556	WCDM [11]	TOG'23	59.420
GUPDM [27]	ACM MM'23	22.372	0.834	0.167	42.313	50.731	0.617	IR-SDE [21]	ICML'23	59.248
WCDM [11]	TOG'23	22.286	0.837	0.197	51.238	48.573	0.611	GSAD [8]	NeurIPS'23	58.969
DA-CLIP [22]	ICLR'24	21.342	0.799	0.209	49.577	47.947	0.578	FourierDiff [23]	CVPR'24	62.259
Ours	-	22.737	0.853	0.141	35.467	51.682	0.666	DA-CLIP [22]	ICLR'24	60.178
								Ours	-	63.846

(a) Underwater image enhancement on the LSUI dataset

(b) Backlight Enhancement on the Backlit300 dataset.

perceptually oriented recovery results compared to the baseline methods. For example, IR-SDE fails to remove and recover specific regions efficiently in the image defogging and image inpainting tasks. DA-CLIP distorts some details in the image inpainting and deblurring tasks, which leads to unsatisfactory visual perceptions. This indicates that CycleRDM achieves effective reconstruction of detail regions in multi-stage refinement.

Table 6: Quantitative comparison of our method with other state-of-the-art methods in the unpaired datasets DICM and LIME. The best and second performance are marked in red and blue, respectively.

Methods	Reference	DICM	LIME
		MUSIQ \uparrow	MUSIQ \uparrow
SNRNet [42]	CVPR'22	53.594	52.165
CLIP-Lit [18]	ICCV'23	63.637	62.865
NeRCo [43]	ICCV'23	63.878	66.122
UHDFour [16]	ICLR'23	59.238	58.125
GDP [3]	CVPR'23	55.134	57.320
GSAD [8]	NeurIPS'23	65.371	59.945
IR-SDE [21]	ICML'23	61.279	55.134
WCDM [11]	TOG'23	58.264	57.617
FourierDiff [23]	CVPR'24	60.882	61.012
DA-CLIP [22]	ICLR'24	63.559	62.516
UPT-Flow [41]	PR'25	62.251	65.564
Ours	-	65.581	66.253

4.4. Image Enhancement Tasks

Encouraged by the excellent performance on the image recovery task, we further evaluate the generalization ability of CycleRDM for more challenging non-linear image enhancement tasks. We demonstrate three enhancement tasks: low-light image enhancement on the LOLv1 [38] and LOLv2.Real [45] datasets, underwater image enhancement on the LSUI dataset [29], and backlight image enhancement on the BackLit300 unpaired dataset [18]. In addition, we add MUSIQ [13] and visual information fidelity(VIF) [33] metrics to evaluate the model performance further. For the unpaired dataset BackLit300, we only use MUSIQ for evaluation.

Comparison Methods. To further validate the model performance, we conducted a comprehensive comparison of three SOTA methods for specific image enhancement tasks. All methods are listed below: SNRNet [42], NeRco [43], CLIP-LIT [18], GDP [3], UHDFour [16], GSAD [8], FourierDiff [23], LightenDiffusion [12], TAFL [19], PUIE-Net [5], USUIR [4], Semi-UIR [9], PUGAN[2], GUPDM [27], WCDM [11], DA-CLIP [22], UPT-Flow [41].

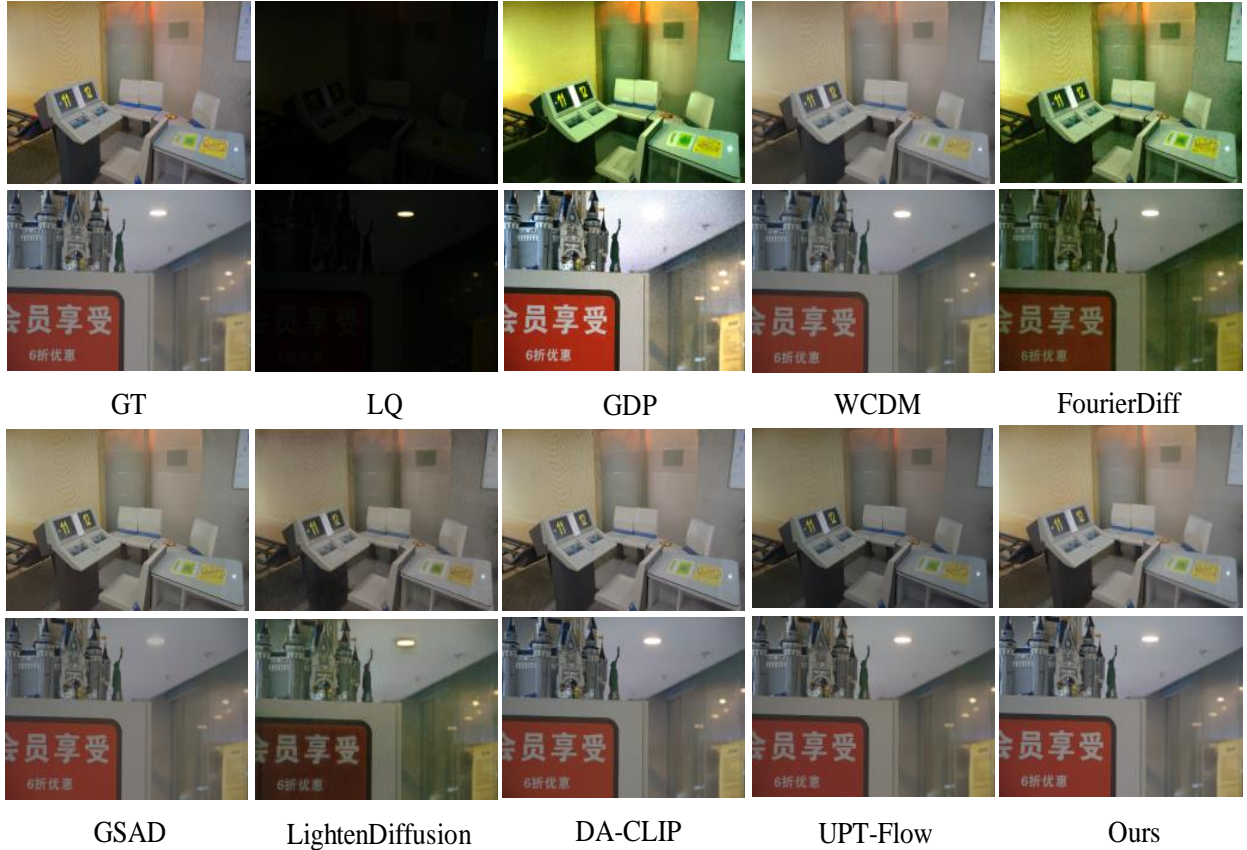


Figure 5: Comparison of our method with competing methods on low light image enhancement task. Best viewed by zooming in.

Quantitative Results. As shown in Table 4, except for the PSNR evaluation, our method obtains the top two evaluation performances on all datasets for other metrics, and in particular for the perception metric MUSIQ, LPIPS and VIF, we redefine the state-of-the-art performance for all datasets. More importantly, the competing methods are focused on augmentation tasks and do not have superior task expansion capabilities. Table 5 shows the performance comparison in the underwater image enhancement and backlight image enhancement tasks. Despite the fact that CycleRDM uses only a small amount of training data, it still obtains excellent performance, obtaining the best evaluations for both tasks. In addition, as shown in Table 6, to further validate the model generalisation ability, we tested it on the unpaired datasets LIME [6] and DICM [14]. It can be clearly seen that CycleRDM

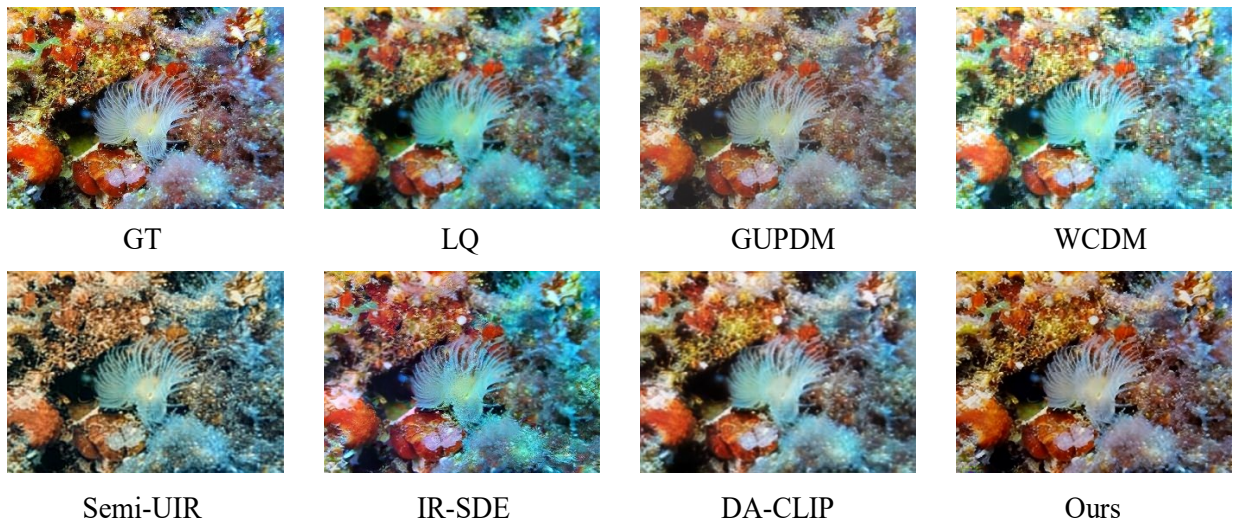


Figure 6: Comparison of our method with other state-of-the-art methods in underwater image enhancement tasks.

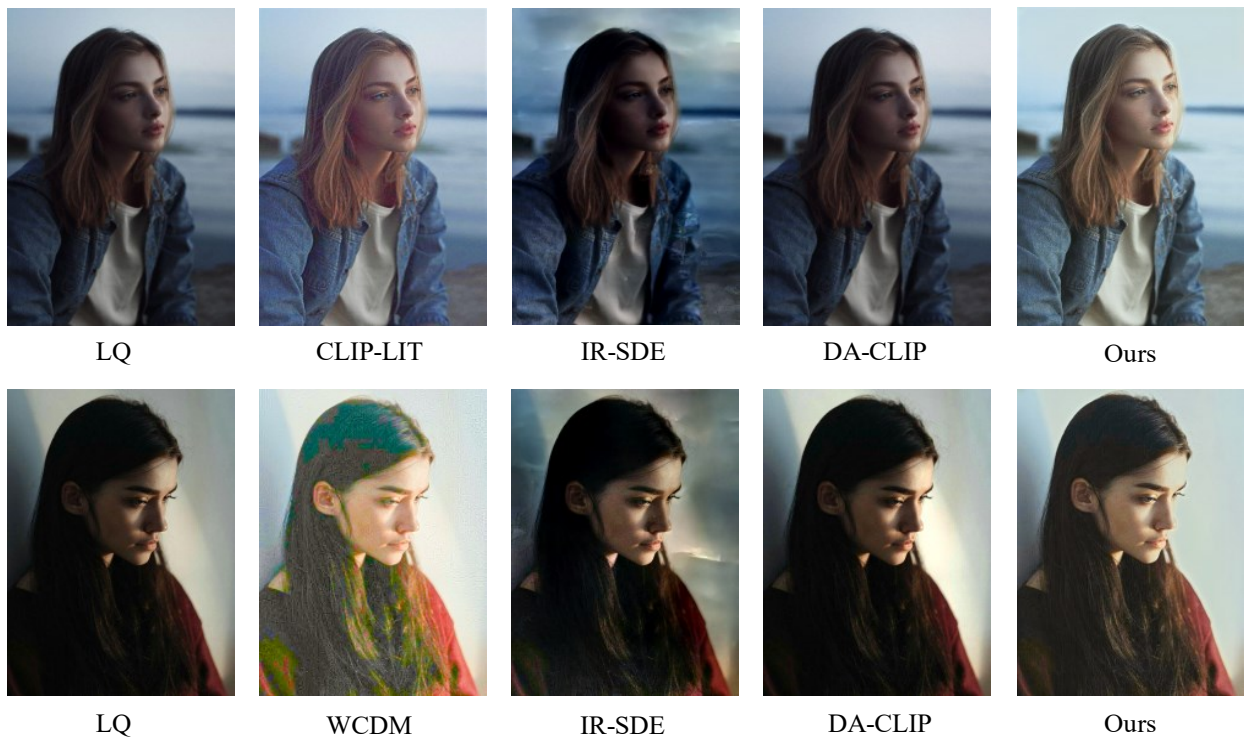


Figure 7: Comparison of our method with other state-of-the-art methods in backlit image enhancement.

acquires the optimal performance, which fully verifies the excellent processing capability of CycleRDM for different scenarios.

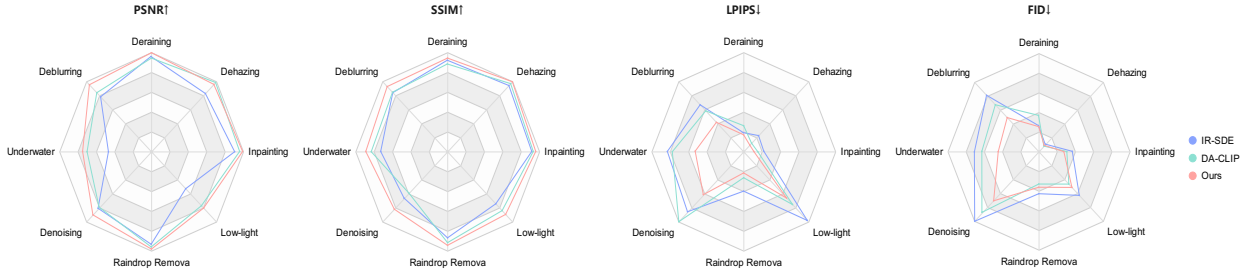


Figure 8: Our method is compared with IR-SDE and DA-CLIP for uniform image recovery. Each radar plot reports results for eight different degradation types for a particular metric. For the perceptual metrics LPIPS and FID, lower values are better.

Qualitative Results. Fig. 5, Fig. 6 and Fig. 7 show visual comparisons in the low-light image enhancement, underwater image enhancement and backlit image enhancement tasks, respectively. Among them, in Fig. 5, we find that FourierDiff and WCDM have some colour distortion. LightenDiffusion and UPT-Flow do not achieve good enhancement. And CyclerRDM can reach an effective balance between colour and luminance as GSAD, so as to obtain a satisfactory visual perception. For the underwater image enhancement task, in Fig. 6 we can easily see that the competing methods do not effectively remove the redundant features and colours of the underwater environment. In contrast, CycleRDM can recover clean and clear images and can achieve excellent detail processing. In addition, from Fig. 7 we see that IR-SDE and DA-CLIP are limited by their insensitivity to the backlighting task, which results in the model not being able to show effective generalisation ability in this task. By comparison, we further confirm the effectiveness of CycleRDM in image enhancement tasks, and we can perfect the unification of linear and blind tasks compared to other single models.

4.5. Detailed Performance Analysis

This subsection compares our method with other unified image restoration methods in detail. As shown in Fig. 8 and Table 7, we summarise in detail the metrics comparison with the two baseline methods, IR-SDE and DA-CLIP, on 8 tasks. In addition, as shown in Table 8, we computed the average metric results of our method and the baseline method on all tasks

Table 7: Here, we also provide a more detailed comparison of our method with other unified image restoration method baselines. The best performance for each metric is **bolded**.

Task	IR-SDE	DA-CLIP	Ours	Task	IR-SDE	DA-CLIP	Ours
Dehazing	25.250	30.062	29.202	Dehazing	0.908	0.935	0.961
Denoising	24.821	24.333	27.424	Denoising	0.641	0.571	0.789
Deblurring	23.723	25.631	29.056	Deblurring	0.806	0.812	0.889
Deraining	29.097	28.756	30.407	Deraining	0.886	0.849	0.908
Inpainting	27.577	29.277	30.292	Inpainting	0.884	0.901	0.926
Raindrop	28.491	29.305	29.857	Raindrop	0.836	0.882	0.908
Low-light	16.072	23.528	24.423	Low-light	0.719	0.811	0.865
Underwater	14.284	21.342	22.737	Underwater	0.699	0.799	0.853
Average	23.664	26.529	27.925	Average	0.797	0.820	0.887

(a) Comparison of our method with the baseline method in PSNR.

(b) Comparison of our method with the baseline method in SSIM.

Task	IR-SDE	DA-CLIP	Ours	Task	IR-SDE	DA-CLIP	Ours
Dehazing	0.062	0.033	0.026	Dehazing	8.330	5.341	7.095
Denoising	0.232	0.269	0.166	Denoising	79.380	69.908	55.947
Deblurring	0.179	0.156	0.113	Deblurring	64.506	53.660	38.643
Deraining	0.050	0.071	0.050	Deraining	20.869	29.214	20.318
Inpainting	0.061	0.042	0.039	Inpainting	29.605	22.684	22.053
Raindrop	0.107	0.061	0.058	Raindrop	34.221	22.379	28.879
Low-light	0.231	0.195	0.168	Low-light	52.466	34.852	41.128
Underwater	0.268	0.209	0.141	Underwater	54.131	49.577	35.467
Average	0.149	0.130	0.095	Average	42.939	35.952	31.191

(c) Comparison of our method with the baseline method in LPIPS.

(d) Comparison of our method with the baseline method in FID.

Table 8: Comparison of the average results over all different datasets on the unified image restoration task.

Methods	Reference	PSNR \uparrow	SSIM \uparrow	LPIPS \downarrow	FID \downarrow
IR-SDE	ICML'23	23.664	0.797	0.149	42.939
DA-CLIP	ICLR'24	26.529	0.820	0.130	35.952
Ours	-	27.925	0.887	0.095	31.191

separately to show more overall performance. It is intuitively clear that DA-CLIP, although it can be optimised to some extent for various degradation tasks, this optimisation does not compete strongly with the current state-of-the-art task-specific methods and, in particular, has significant drawbacks in terms of distortion metrics. Meanwhile, compared with IR-SDE based on the diffusion model, attributed to the multi-level refinement of image restoration, we have greatly narrowed the performance gap between the various tasks, and achieved a perfect balance of the diffusion model between the image restoration and enhancement tasks, which leads to a more stable restoration result of the model. Among them, compared with IR-SDE and DA-CLIP, we have risen **4.261 dB** and **1.396 dB** in PSNR evaluation, respectively. in SSIM, we have **0.09** and **0.067** rise. For the distortion metrics LPIPS and FID, we also have a significant lead with **0.054/0.035** and **11.748/4.761** uplifts, respectively.

4.6. Ablation Study

In this subsection, we conduct a series of ablation studies to measure the impact of the different component configurations employed in our approach. Specific details are given below:

The Effectiveness of the Multi-stage inference process. ablation experiments on a low-light enhancement task, we verified their effectiveness. As shown in Table 9, where #1 denotes single-stage inference using only Stage1, #2 does not perform the final wavelet calibration process, #3 does not perform the rough normal-domain-to-normal-domain learning process, and #4 uses the full setup. We can see that both #2 and #3 obtain significant performance gains compared to single-stage inference #1, especially for the PSNR evaluation, which obtains 2.293 dB and 3.031 dB, respectively, but degrades for the perceptual metric FID. To further refine the degraded domain, we applied the default setting of configuration #4. Among the four model configurations, #4 achieved the best evaluation results, demonstrating a notable improvement. Specifically, it enhanced the PSNR metric by an additional 1.246 dB compared to configuration #3, while simultaneously alleviating the perceptual metric degradation in FID. These results validate that the refined multi-stage degradation

Table 9: Ablation studies of multi-stage inference process.

index	Stage 1	Stage 2	Stage 3	PSNR \uparrow	SSIM \uparrow	LPIPS \downarrow	FID \downarrow
#1	✓	✗	✗	20.146	0.835	0.201	41.059
#2	✓	✓	✗	22.439	0.848	0.198	46.213
#3	✓	✗	✓	23.177	0.854	0.191	46.998
#4	✓	✓	✓	24.423	0.865	0.179	41.128

Table 10: Ablation studies of the Feature Gain Module.

version	PSNR \uparrow	SSIM \uparrow	LPIPS \downarrow	FID \downarrow
CycleRDM	27.655	0.952	0.027	6.906
CycleRDM+FGM	29.202	0.960	0.026	7.095

Table 11: Ablation studies of the loss function terms.

Setting	PSNR \uparrow	SSIM \uparrow	LPIPS \downarrow	FID \downarrow
without \mathcal{L}_{diff}	28.131	0.895	0.098	82.892
without $\mathcal{L}_{content}$	25.478	0.853	0.101	68.103
without \mathcal{L}_{fre}	28.979	0.902	0.065	35.151
without \mathcal{L}_{clip}	28.305	0.900	0.061	31.205
Default	29.857	0.908	0.058	28.879

priors, in conjunction with the calibration process, significantly enhanced the mapping quality from the degraded domain to the normal domain. This underscores the effectiveness of the proposed CycleRDM framework.

The Effectiveness of the Feature Gain Module. We use the image dehazing task for validation, as shown in Table 10, after adding the FGM on top of CycleRDM, the model improves in the distortion metrics, which indicates that the feature gain module can effectively remove the redundant features in the wavelet high-frequency information, which prompts the output results to be closer to the normal image.

The Effectiveness of the Loss Function. We also verify the validity of the proposed loss function in this subsection, where we perform the experiments by removing each component individually from the default settings, and the quantitative results are reported in Table 11. As shown in row 1, deleting the diffusion loss \mathcal{L}_{diff} leads to a significant reduction in the perceptual metrics, and the generative power of the diffusion model relies heavily on this component. The content loss $\mathcal{L}_{content}$ produces a noticeable change in the image generation results, especially in the distortion metrics, which can be improved by 4.379dB and 0.055 for PSNR and SSIM, respectively. The frequency domain perceptual loss \mathcal{L}_{fre} and the multimodal text loss \mathcal{L}_{clip} are intended to further aid in the reconstruction of image details and stabilize diffusion content generation, so its removal results in performance degradation. However, their degradation is significantly smaller than the diffusion loss and content loss. Thus, this reveals the importance of diffusion loss and content loss. From another perspective, the fact that content and diffusion loss should be combined with our proposed multi-stage diffusion inference training strategy illustrates their effectiveness.

5. LIMITATION AND FUTURE WORK

Since degradation datasets mostly contain only a single degradation label for each image, our current model has not been trained to recover multiple degradations in the same scene. Although we have demonstrated the performance stability and generalization capabilities of CycleRDM when extended for degradation tasks, this limitation has prevented us from effectively exploring recovery capabilities for realistic mixed degradation scenes.

To address the above issues, in our future work, we will further explore the following aspects: 1) creating hybrid datasets containing multiple degraded scenes; 2) further exploring the real-time performance of the diffusion model for the task of unified image recovery; and 3) exploring further effective combinations of multimodal and diffusion models when dealing with degradation tasks.

6. CONCLUSIONS

In this paper, we propose CycleRDM, a novel framework designed to unify image restoration and enhancement tasks efficiently. CycleRDM employs a multilevel inference process to achieve high-quality mappings from degraded domains while progressively optimizing image details to ensure robust generalization. To further enhance its performance, we introduce a feature gain module that refines image restoration by effectively eliminating redundant features. Moreover, multimodal textual prompts are incorporated to positively guide the generation process, significantly boosting its recovery capabilities. Tested across nine tasks, CycleRDM delivers efficient and high-quality results using only a limited amount of training data, demonstrating its versatility and effectiveness in unifying image restoration and enhancement tasks.

References

- [1] Liangyu Chen, Xiaojie Chu, Xiangyu Zhang, and Jian Sun. Simple baselines for image restoration. In *European conference on computer vision*, pages 17–33. Springer, 2022.
- [2] Runmin Cong, Wenyu Yang, Wei Zhang, Chongyi Li, Chun-Le Guo, Qingming Huang, and Sam Kwong. Pugan: Physical model-guided underwater image enhancement using gan with dual-discriminators. *IEEE Transactions on Image Processing*, 2023.
- [3] Ben Fei, Zhaoyang Lyu, Liang Pan, Junzhe Zhang, Weidong Yang, Tianyue Luo, Bo Zhang, and Bo Dai. Generative diffusion prior for unified image restoration and enhancement. In *Proceedings of the IEEE/CVF Conference on Computer Vision and Pattern Recognition*, pages 9935–9946, 2023.
- [4] Zhenqi Fu, Huangxing Lin, Yan Yang, Shu Chai, Liyan Sun, Yue Huang, and Xinghao Ding. Unsupervised underwater image restoration: From a homology perspective. In *Proceedings of the AAAI Conference on Artificial Intelligence*, volume 36, pages 643–651, 2022.
- [5] Zhenqi Fu, Wu Wang, Yue Huang, Xinghao Ding, and Kai-Kuang Ma. Uncertainty inspired underwater image enhancement. In *European conference on computer vision*, pages 465–482. Springer, 2022.
- [6] Xiaojie Guo, Yu Li, and Haibin Ling. Lime: Low-light image enhancement via illumination map estimation. *IEEE Transactions on image processing*, 26(2):982–993, 2016.
- [7] Martin Heusel, Hubert Ramsauer, Thomas Unterthiner, Bernhard Nessler, and Sepp Hochreiter. Gans trained by a two time-scale update rule converge to a local nash equilibrium. *Advances in neural information processing systems*, 30, 2017.

- [8] Jinhui Hou, Zhiyu Zhu, Junhui Hou, Hui Liu, Huanqiang Zeng, and Hui Yuan. Global structure-aware diffusion process for low-light image enhancement. *Advances in Neural Information Processing Systems*, 36, 2024.
- [9] Shirui Huang, Keyan Wang, Huan Liu, Jun Chen, and Yunsong Li. Contrastive semi-supervised learning for underwater image restoration via reliable bank. In *Proceedings of the IEEE/CVF conference on computer vision and pattern recognition*, pages 18145–18155, 2023.
- [10] Yi Huang, Jiancheng Huang, Jianzhuang Liu, Mingfu Yan, Yu Dong, Jiayi Lyu, Chaoqi Chen, and Shifeng Chen. Wavedm: Wavelet-based diffusion models for image restoration. *IEEE Transactions on Multimedia*, 2024.
- [11] Hai Jiang, Ao Luo, Haoqiang Fan, Songchen Han, and Shuaicheng Liu. Low-light image enhancement with wavelet-based diffusion models. *ACM Transactions on Graphics (TOG)*, 42(6):1–14, 2023.
- [12] Hai Jiang, Ao Luo, Xiaohong Liu, Songchen Han, and Shuaicheng Liu. Lightendiffusion: Unsupervised low-light image enhancement with latent-retinex diffusion models. *arXiv preprint arXiv:2407.08939*, 2024.
- [13] Junjie Ke, Qifei Wang, Yilin Wang, Peyman Milanfar, and Feng Yang. Musiq: Multi-scale image quality transformer. In *Proceedings of the IEEE/CVF international conference on computer vision*, pages 5148–5157, 2021.
- [14] Chulwoo Lee, Chul Lee, and Chang-Su Kim. Contrast enhancement based on layered difference representation of 2d histograms. *IEEE transactions on image processing*, 22(12):5372–5384, 2013.
- [15] Boyun Li, Xiao Liu, Peng Hu, Zhongqin Wu, Jiancheng Lv, and Xi Peng. All-in-one image restoration for unknown corruption. In *Proceedings of the IEEE/CVF Conference on Computer Vision and Pattern Recognition*, pages 17452–17462, 2022.
- [16] Chongyi Li, Chun-Le Guo, Man Zhou, Zhexin Liang, Shangchen Zhou, Ruicheng Feng, and Chen Change Loy. Embedding fourier for ultra-high-definition low-light image enhancement. *arXiv preprint arXiv:2302.11831*, 2023.
- [17] Dasong Li, Yi Zhang, Ka Chun Cheung, Xiaogang Wang, Hongwei Qin, and Hongsheng Li. Learning degradation representations for image deblurring. In *European Conference on Computer Vision*, pages 736–753. Springer, 2022.
- [18] Zhexin Liang, Chongyi Li, Shangchen Zhou, Ruicheng Feng, and Chen Change Loy. Iterative prompt learning for unsupervised backlit image enhancement. In *Proceedings of the IEEE/CVF International Conference on Computer Vision*, pages 8094–8103, 2023.
- [19] Risheng Liu, Zhiying Jiang, Shuzhou Yang, and Xin Fan. Twin adversarial contrastive learning for underwater image enhancement and beyond. *IEEE Transactions on Image Processing*, 31:4922–4936, 2022.

- [20] Andreas Lugmayr, Martin Danelljan, Andres Romero, Fisher Yu, Radu Timofte, and Luc Van Gool. Repaint: Inpainting using denoising diffusion probabilistic models. In *Proceedings of the IEEE/CVF conference on computer vision and pattern recognition*, pages 11461–11471, 2022.
- [21] Ziwei Luo. Image restoration with mean-reverting stochastic differential equations. In *International Conference on Machine Learning (ICML)*, 2023.
- [22] Ziwei Luo, Fredrik K. Gustafsson, Zheng Zhao, Jens Sjölund, and Thomas B. Schön. Controlling vision-language models for multi-task image restoration. In *The Twelfth International Conference on Learning Representations*, 2024.
- [23] Xiaoqian Lv, Shengping Zhang, Chenyang Wang, Yichen Zheng, Bineng Zhong, Chongyi Li, and Liqiang Nie. Fourier priors-guided diffusion for zero-shot joint low-light enhancement and deblurring. In *Proceedings of the IEEE/CVF Conference on Computer Vision and Pattern Recognition*, pages 25378–25388, 2024.
- [24] Haoyu Ma, Shaojun Liu, Qingmin Liao, Juncheng Zhang, and Jing-Hao Xue. Defocus image deblurring network with defocus map estimation as auxiliary task. *IEEE Transactions on Image Processing*, 31:216–226, 2021.
- [25] Xintian Mao, Yiming Liu, Fengze Liu, Qingli Li, Wei Shen, and Yan Wang. Intriguing findings of frequency selection for image deblurring. In *Proceedings of the AAAI Conference on Artificial Intelligence*, volume 37, pages 1905–1913, 2023.
- [26] David Martin, Charless Fowlkes, Doron Tal, and Jitendra Malik. A database of human segmented natural images and its application to evaluating segmentation algorithms and measuring ecological statistics. In *Proceedings Eighth IEEE International Conference on Computer Vision. ICCV 2001*, volume 2, pages 416–423. IEEE, 2001.
- [27] Pan Mu, Hanning Xu, Zheyuan Liu, Zheng Wang, Sixian Chan, and Cong Bai. A generalized physical-knowledge-guided dynamic model for underwater image enhancement. In *Proceedings of the 31st ACM International Conference on Multimedia*, pages 7111–7120, 2023.
- [28] Dongwon Park, Dong Un Kang, Jisoo Kim, and Se Young Chun. Multi-temporal recurrent neural networks for progressive non-uniform single image deblurring with incremental temporal training. In *European Conference on Computer Vision*, pages 327–343. Springer, 2020.
- [29] Lintao Peng, Chunli Zhu, and Liheng Bian. U-shape transformer for underwater image enhancement. *IEEE Transactions on Image Processing*, 2023.
- [30] Rui Qian, Robby T Tan, Wenhan Yang, Jiajun Su, and Jiaying Liu. Attentive generative adversarial network for raindrop removal from a single image. In *Proceedings of the IEEE conference on computer vision and pattern recognition*, pages 2482–2491, 2018.
- [31] Xu Qin, Zhilin Wang, Yuanchao Bai, Xiaodong Xie, and Huizhu Jia. Ffa-net: Feature fusion attention

- network for single image dehazing. In *Proceedings of the AAAI conference on artificial intelligence*, volume 34, pages 11908–11915, 2020.
- [32] Dongwei Ren, Wei Shang, Pengfei Zhu, Qinghua Hu, Deyu Meng, and Wangmeng Zuo. Single image deraining using bilateral recurrent network. *IEEE Transactions on Image Processing*, 29:6852–6863, 2020.
- [33] H Sheikh. Live image quality assessment database release 2. <http://live.ece.utexas.edu/research/quality>, 2005.
- [34] Hang Sun, Zhiming Luo, Dong Ren, Bo Du, Laibin Chang, and Jun Wan. Unsupervised multi-branch network with high-frequency enhancement for image dehazing. *Pattern Recognition*, 156:110763, 2024.
- [35] Chunwei Tian, Menghua Zheng, Wangmeng Zuo, Bob Zhang, Yanning Zhang, and David Zhang. Multi-stage image denoising with the wavelet transform. *Pattern Recognition*, 134:109050, 2023.
- [36] Zhengzhong Tu, Hossein Talebi, Han Zhang, Feng Yang, Peyman Milanfar, Alan Bovik, and Yinxiao Li. Maxim: Multi-axis mlp for image processing. In *Proceedings of the IEEE/CVF conference on computer vision and pattern recognition*, pages 5769–5780, 2022.
- [37] Zhou Wang, Alan C Bovik, Hamid R Sheikh, and Eero P Simoncelli. Image quality assessment: from error visibility to structural similarity. *IEEE transactions on image processing*, 13(4):600–612, 2004.
- [38] Chen Wei, Wenjing Wang, Wenhan Yang, and Jiaying Liu. Deep retinex decomposition for low-light enhancement. *arXiv preprint arXiv:1808.04560*, 2018.
- [39] Xiaohe Wu, Ming Liu, Yue Cao, Dongwei Ren, and Wangmeng Zuo. Unpaired learning of deep image denoising. In *European conference on computer vision*, pages 352–368. Springer, 2020.
- [40] Jie Xiao, Xueyang Fu, Aiping Liu, Feng Wu, and Zheng-Jun Zha. Image de-raining transformer. *IEEE Transactions on Pattern Analysis and Machine Intelligence*, 2022.
- [41] Lintao Xu, Changhui Hu, Yin Hu, Xiaoyuan Jing, Ziyun Cai, and Xiaobo Lu. Upt-flow: Multi-scale transformer-guided normalizing flow for low-light image enhancement. *Pattern Recognition*, 158:111076, 2025.
- [42] Xiaogang Xu, Ruixing Wang, Chi-Wing Fu, and Jiaya Jia. Snr-aware low-light image enhancement. In *Proceedings of the IEEE/CVF conference on computer vision and pattern recognition*, pages 17714–17724, 2022.
- [43] Shuzhou Yang, Moxuan Ding, Yanmin Wu, Zihan Li, and Jian Zhang. Implicit neural representation for cooperative low-light image enhancement. In *Proceedings of the IEEE/CVF International Conference on Computer Vision*, pages 12918–12927, 2023.
- [44] Wenhan Yang, Robby T Tan, Jiashi Feng, Jiaying Liu, Zongming Guo, and Shuicheng Yan. Deep joint rain detection and removal from a single image. In *Proceedings of the IEEE conference on computer vision and pattern recognition*, pages 1357–1366, 2017.

- [45] Wenhan Yang, Wenjing Wang, Haofeng Huang, Shiqi Wang, and Jiaying Liu. Sparse gradient regularized deep retinex network for robust low-light image enhancement. *IEEE Transactions on Image Processing*, 30:2072–2086, 2021.
- [46] Yang Yang, Chaoyue Wang, Xiaojie Guo, and Dacheng Tao. Robust unpaired image dehazing via density and depth decomposition. *International Journal of Computer Vision*, pages 1–21, 2023.
- [47] Yang Yang, Chaoyue Wang, Risheng Liu, Lin Zhang, Xiaojie Guo, and Dacheng Tao. Self-augmented unpaired image dehazing via density and depth decomposition. In *Proceedings of the IEEE/CVF conference on computer vision and pattern recognition*, pages 2037–2046, 2022.
- [48] Nana Yu, Jie Wang, Hong Shi, Zihao Zhang, and Yahong Han. Degradation-removed multiscale fusion for low-light salient object detection. *Pattern Recognition*, page 110650, 2024.
- [49] Syed Waqas Zamir, Aditya Arora, Salman Khan, Munawar Hayat, Fahad Shahbaz Khan, and Ming-Hsuan Yang. Restormer: Efficient transformer for high-resolution image restoration. In *Proceedings of the IEEE/CVF conference on computer vision and pattern recognition*, pages 5728–5739, 2022.
- [50] Syed Waqas Zamir, Aditya Arora, Salman Khan, Munawar Hayat, Fahad Shahbaz Khan, Ming-Hsuan Yang, and Ling Shao. Multi-stage progressive image restoration. In *Proceedings of the IEEE/CVF conference on computer vision and pattern recognition*, pages 14821–14831, 2021.
- [51] Richard Zhang, Phillip Isola, Alexei A Efros, Eli Shechtman, and Oliver Wang. The unreasonable effectiveness of deep features as a perceptual metric. In *Proceedings of the IEEE conference on computer vision and pattern recognition*, pages 586–595, 2018.
- [52] Ronghui Zhang, Jiongze Yu, Junzhou Chen, Guofa Li, Liang Lin, and Danwei Wang. A prior guided wavelet-spatial dual attention transformer framework for heavy rain image restoration. *IEEE Transactions on Multimedia*, 2024.
- [53] Hongyi Zheng, Hongwei Yong, and Lei Zhang. Deep convolutional dictionary learning for image denoising. In *Proceedings of the IEEE/CVF conference on computer vision and pattern recognition*, pages 630–641, 2021.
- [54] Zhihang Zhong, Ye Gao, Yinqiang Zheng, Bo Zheng, and Imari Sato. Real-world video deblurring: A benchmark dataset and an efficient recurrent neural network. *International Journal of Computer Vision*, 131(1):284–301, 2023.
- [55] Xinshan Zhu, Shuoshi Li, Yongdong Gan, Yun Zhang, and Biao Sun. Multi-stream fusion network with generalized smooth l_1 loss for single image dehazing. *IEEE Transactions on Image Processing*, 30:7620–7635, 2021.